 CMES, vol.95, no.1, pp.59-85, 2013

Modeling and Simulation of Non-Newtonian Fluid Mold Filling Process with Phase Change

F. Wang[1], J.L. Li[1], B.X. Yang[1] and N.A. Hill[2]

Abstract: A gas-liquid two-phase model for the simulation of a power-law fluid mold filling process with the consideration of phase change is proposed, in which the governing equations for the melt and air in the cavity, including the mass conservation, momentum conservation and energy conservation equations, are unified into one system of equation. A revised Enthalpy method, which can be used for both the melt and air in the mold cavity, is proposed to describe the phase change during the mold filling. Finite volume method on non-staggered grid is used to solve the system. The level set method is used to capture the interface evolution during the mold filling process. The interface evolution and the distributions of physical quantities such as velocity, pressure and temperature and so on are given. The "frozen skin" layers under different temperature and velocities conditions are discussed in detail. Numerical results show that increasing the temperatures of the melt and cavity is a better way to get rid of the "frozen skin" layer than increasing the injection velocity.

Keywords: Mold filling, non-isothermal, non-Newtonian flow, phase change, Enthalpy method.

1 Introduction

In mold filling process, plastic material in the form of granules is melted until soft enough to be injected under pressure to fill a mold. Some researchers have studied the mold filling process numerically from Hele-Shaw model to Navier-Stokes equations without the consideration of the interface motion [Wang, Hieber, and Wang (1986); Chiang, Hieber, and Wang (1991); Kabanemi, Vaillancourt, Wang, and Salloum (1998); Smith, Tortorelli, and Tucker (1998); Hetu, Gao, Garcia-Rejon, and Salloum (1998); Pichelin and Coupez (1998); Kim and Turng (2006); Zhou, Geng,

[1] School of Applied Sciences, Taiyuan University of Science and Technology, Taiyuan, Shanxi, P.R. China
[2] School of Mathematics and Statistics, University of Glasgow, Glasgow, U.K.

and Li (2005); Chang and Yang (2001); Zhou and Turng (2007)]. Some papers studying mold filling process coupled with interface tracking techniques or computer aided design can be found [Khayat, Elsin, and Kim (2000); Holm and Langtangen (1999); Luoma and Voller (2000); Soukane and Trochu (2006); Ayad and Rigolot (2002); Geng, Li, and Zhou (2006); Kim, Park, and Lee (2003); Zhou, Yan, and Zhang (2008); Au (2005); Khor, Ariff, Ani, Mujeebu, Abdullah, Abdullah, and Joseph (2010); Yang, Ouyang, Liu, and Li (2010); Yang, Ouyang, Jiang, and Liu (2010); Li, Ouyang, Li, Wu, and Yang (2011); Wang, Andres, Simacek, and Advani (2012)]. However, these papers studied the mold filling problem by ignoring the temperature variation. As a matter of fact, the temperature on the side walls of the mold cavity is much lower than that of the melt. As a result, near the mold walls, the viscosity is higher due to the decreased temperature. The polymer tends to solidify as the viscosity increases, which is known as phase change or "frozen skin" layer. Meanwhile, great amount of heat, known as latent heat, will be released at the moment that the melt begins to solidify. The latent heat will stop the melt from solidifying. Since "frozen skin" layer is not desirable because it contributes to the "molded in" strains in the molded article, the phase change and the temperature variation should be studied carefully. However, to the knowledge of all the authors, no such paper considering the phase change and latent heat in the mold filling process has ever been published.

In this paper, a model for the simulation of a power-law fluid mold filling process with the consideration of phase change is proposed. To avoid dealing with the complex boundary conditions at the melt interface, we consider simultaneously both the melt phase and the gas phase in the cavity as has been done by Yang, Ouyang, Liu, and Li (2010). The governing equations for the melt and air in the cavity, including the mass conservation, momentum conservation and energy conservation equations, are unified into one system of equation. A finite volume method on non-staggered grid is used to solve the system. The level set method is used to capture the interface evolution during the mold filling process. In order to describe the phase change during the mold filling process, a revised Enthalpy method, which can be used for both the melt and air in the mold cavity, is proposed to describe the phase change during the mold filling. The "frozen skin" layers under different temperature and velocities conditions are discussed in detail.

2 Governing equations

2.1 Level set function and its reinitialization [Yang, Ouyang, Liu, and Li (2010)]

The basic idea of the level set method is to indicate the interface implicitly by a level set function $\varphi(x,y,t)$, which is defined by the algebraic distance between any

point of the domain and the melt flow front. The melt flow front is thus described by the zero level sets of the level set function φ. In this paper, the level set equation is chosen as the follows [Osher and Fedkiw (2001)].

$$\frac{\partial \varphi}{\partial t} + \mathbf{u} \cdot \nabla \varphi = 0 \tag{1}$$

where $\mathbf{u}$ is the velocity vector.

Moreover, a reinitialization algorithm must be applied to keep φ as the algebraic distance to the interface. The algorithm is based on the iterative solution of the following initial value problem [Osher and Fedkiw (2001)]

$$\begin{cases} \frac{\partial \varphi}{\partial t_r} = \text{sign}\varphi_0(1 - |\nabla \varphi|) \\ \varphi(x,0) = \varphi_0(x) \end{cases} \tag{2}$$

where t_r is a pseudo time and $\text{sign}(\varphi_0)$ is the sign function of which is defined as

$$\text{sign}(\varphi_0) = \frac{\varphi_0}{\sqrt{\varphi_0^2 + [\min(\Delta x, \Delta y)]^2}} \tag{3}$$

where Δx and Δy are the grid widths along the x and y direction respectively. $[\min(\Delta x, \Delta y)]^2$ is used here to avoid denominator being dividing by zero.

Eq. (2)does not change the position of the zero level set of φ. Unfortunately in numerical computation this may not be true [Sussman, Fatemi, Smereka, and Osher (1998)]. We use the method presented by Sussman, Fatemi, Smereka, and Osher (1998) to improve the accuracy of solving the reinitialization equation. A local correction item, $\theta \delta_\varepsilon(\varphi)|\Delta\varphi|$, is added to the reinitialization equation (2), thus the revised equation is

$$\frac{\partial \varphi}{\partial t_r} + \text{sign}(\varphi_0)(|\Delta\varphi| - 1) = \theta \delta_\varepsilon(\varphi)|\Delta\varphi| \tag{4}$$

where θ is a local correction coefficient and the smoothed Dirac delta function $\delta_\varepsilon(\varphi)$ is defined as

$$\delta_\varepsilon(\varphi) = \begin{cases} \frac{1}{2\varepsilon}\left(1 + \cos\left(\frac{\pi\varphi}{\varepsilon}\right)\right), & |\varphi| < \varepsilon \\ 0, & \text{otherwise} \end{cases} \tag{5}$$

Here, ε is the thickness of the interface that is proportional to the spatial mesh. See Sussman, Fatemi, Smereka, and Osher (1998) for more details.

2.2 Governing equations for the fluid

Both the gas phase and the liquid melt are regarded as incompressible and two phases are treated in a single Eulerian grid by the level set method.

The governing equations for the melt in the cavity are

$$\nabla \cdot \mathbf{u} = 0 \tag{6}$$

$$\frac{\partial}{\partial t}(\rho_m \mathbf{u}) + \nabla \cdot (\rho_m \mathbf{u}\mathbf{u}) = -\nabla p + \nabla \cdot (2\eta_m \mathbf{D}) \tag{7}$$

$$\frac{\partial}{\partial t}(\rho_m C_m T) + \nabla \cdot (\rho_m C_m \mathbf{u} T) = \nabla \cdot (k_m \nabla T) + \boldsymbol{\sigma} : \mathbf{D} \tag{8}$$

where $\mathbf{u} = (u, v)^T$ is the velocity vector, T is the temperature, p is the pressure, ρ is the density, η is the viscosity, k is the thermal conductivity, C is the specific heat, $\boldsymbol{\sigma}$ is the Cauchy stress tensor, $\boldsymbol{\sigma} = -p\mathbf{I} + \eta\mathbf{D}$, $\mathbf{I}$ is the unit tensor, $\mathbf{D}$ is the strain tensor, and the subscript m represents the melt phase.

The continuity equation for the gas is the same as (6), and the momentum and energy equations for the gas in the cavity are

$$\frac{\partial}{\partial t}(\rho_g \mathbf{u}) + \nabla \cdot (\rho_g \mathbf{u}\mathbf{u}) = -\nabla p + \nabla \cdot (2\eta_g \mathbf{D}) \tag{9}$$

$$\frac{\partial}{\partial t}(\rho_g C_g T) + \nabla \cdot (\rho_g C_g \mathbf{u} T) = \nabla \cdot (k_g \nabla T) + \boldsymbol{\sigma} : \mathbf{D} \tag{10}$$

where the subscript g represents the gas phase in the cavity.

The boundary conditions at the interface between the phases are

$$2\mathbf{n}(\eta_m \mathbf{D} - \eta_g \mathbf{D}) = (p_m - p_g)\mathbf{n} \tag{11a}$$

$$\mathbf{u}_m = \mathbf{u}_g \text{ and } T_m = T_g \tag{11b}$$

where $\mathbf{n}$ is the unit normal to the interface drawn outwards from the liquid to the gas.

Define the Heaviside function as

$$H_\varepsilon(\varphi) = \begin{cases} 0, & \varphi < -\varepsilon \\ \frac{1}{2}\left[1 + \frac{\varphi}{\varepsilon} + \frac{\sin\left(\frac{\pi\varphi}{\varepsilon}\right)}{\pi}\right], & |\varphi| \le \varepsilon \\ 1, & \varphi > \varepsilon \end{cases} \tag{12}$$

Let

$$\rho(\varphi) = \rho_g + (\rho_m - \rho_g)H_\varepsilon(\varphi) \tag{13}$$
$$\eta(\varphi) = \eta_g + (\eta_m - \eta_g)H_\varepsilon(\varphi) \tag{14}$$
$$C(\varphi) = C_g + (C_m - C_g)H_\varepsilon(\varphi) \tag{15}$$
$$k(\varphi) = k_g + (k_m - k_g)H_\varepsilon(\varphi) \tag{16}$$

Then the governing equations for the two-phase flow, along with the boundary conditions (11) can be written as a united generalized Navier-Stokes system, the continuity equation, momentum equation and energy equation are given as below:

$$\frac{\partial \rho}{\partial t} + \nabla \cdot (\rho \mathbf{u}) = 0 \tag{17}$$
$$\frac{\partial}{\partial t}(\rho \mathbf{u}) + \nabla \cdot (\rho \mathbf{u}\mathbf{u}) = -\nabla p + \nabla \cdot (2\eta \mathbf{D}) \tag{18}$$
$$\frac{\partial}{\partial t}(\rho C T) + \nabla \cdot (p C \mathbf{u} T) = \nabla \cdot (k \nabla T) + \boldsymbol{\sigma} : \mathbf{D} \tag{19}$$

Notice that in Eq. (17), the density ρ cannot be omitted because the values of ρ may be different on the two sides of the interface.

Eqs. (17)-(19) can be written in the dimensionless form by introducing the dimensionless variables $x = Lx'$, $y = Ly'$, $u = Uu'$, $v = Uv'$, $t = (L/U)t'$, $p = p_m U^2 p'$, $\rho = \rho_m \rho'$, $\eta = \eta_m \eta'$, $C = C_m C'$, $k = k_m k'$, $T = T_0 T'$, where the primes denote dimensionless variables.

Substituting these dimensionless variables into Eqs. (17)-(19) and dropping the primes, we have

$$\frac{\partial \rho}{\partial t} + \nabla \cdot (\rho \mathbf{u}) = 0 \tag{20}$$
$$\frac{\partial}{\partial t}(\rho \mathbf{u}) + \nabla \cdot (\rho \mathbf{u}\mathbf{u}) = -\nabla p + \frac{1}{Re}\nabla \cdot (2\eta \mathbf{D}) \tag{21}$$
$$Pe\left(\frac{\partial}{\partial t}(\rho C T) + \nabla \cdot (\rho C \mathbf{u} T)\right) - \nabla \cdot (k \nabla T) = Br(\boldsymbol{\sigma} : \mathbf{D}) \tag{22}$$

where Reynolds number $Re = \rho_m LU/\eta_m$, Peclet number $Pe = \rho_m C_m LU/k_m$, Brinkman number $Br = \eta_m U^2/(k_m T_0)$ and

$$\rho(\varphi) = \rho_g/\rho_m + (1 - \rho_g/\rho_m)H_\varepsilon(\varphi) \tag{23}$$
$$\eta(\varphi) = \eta_g/\eta_m + (1 - \eta_g/\eta_m)H_\varepsilon(\varphi) \tag{24}$$
$$C(\varphi) = C_g/C_m + (1 - C_g/C_m)H_\varepsilon(\varphi) \tag{25}$$
$$k(\varphi) = k_g/k_m + (1 - k_g/k_m)H_\varepsilon(\varphi) \tag{26}$$

2.3 Phase change model

Since the temperature on the side walls of the mold cavity is much lower than that of the melt, the polymer tends to solidify near the solid walls of the cavity, which is known as the phase change or "frozen skin" layer. Latent heat must be considered in the phase change because great amount of heat will be released at the moment that the melt begins to solidify. Different models or methods have been proposed to describe phase change, such as the Stefan Model [Rubinstein (1994); Carslaw and Jaeger (1959)], the Enthalpy method [Yang, Fu, Yang, Huang, Yang, and Feng (2008); Krabbenhoft, Damkilde, and Nazem (2007); Kim, Kim, and Chun (2001); Caldwell and Date (2003); Luoma and Voller (2000); Cao, Faghri, and Chang (1989)] and the phase-field method [Cahn and Hilliard (1958)]. One reason for the establishment of the Enthalpy method is to avoid capturing the interface between the solid and liquid during solidification and the Enthalpy can be calculated on fixed grids. The other contribution of the Enthalpy method is the introduction of a narrow mush area between the solid and liquid areas, which takes the position of the mutation interface so that singularities at the interface are removed. In this paper, we set up the model with the consideration of latent heat using the Enthalpy Method. Since we consider simultaneously the polymer melt and the air in the cavity, the Enthalpy model must include the relationship between Enthalpy H and temperature T for both melt phase and air phase. A modified Enthalpy model is proposed in this paper as follows based on the work of Yang et al. [Yang, Fu, Yang, Huang, Yang, and Feng (2008)]

Define $C(T) = \frac{\partial H}{\partial T}$, and the transformation relationship between Enthalpy H and temperature T is given as follows.

$$T(H) = \begin{cases} T_s + \frac{H}{C_s}, & H \leq 0 \\ T_s + \frac{H(T_l - T_s)}{L_H + C_f(T_l - T_s)}, & 0 < H < L_H + C_f(T_l - T_s) \\ T_s + \frac{H}{C_l} - \frac{L_H + (C_f - C_l)(T_l - T_s}{C_l}, & H \geq L_H + C_f(T_l - T_s) \end{cases} \tag{27}$$

Here, L_H is the latent heat, we have

$$T_s = T_g + (T_{m,s} - T_g)H_\varepsilon(\varphi) \tag{28}$$

$$T_l = T_g + (T_{m,l} - T_g)H_\varepsilon(\varphi) \tag{29}$$

$$L_H = L_g + (L_m - L_g)H_\varepsilon(\varphi) \tag{30}$$

$$C_s = C_g + (C_{m,s} - C_g)H_\varepsilon(\varphi) \tag{31}$$

$$C_f = C_g + (C_{m,f} - C_g)H_\varepsilon(\varphi) \tag{32}$$

$$C_l = C_g + (C_{m,l} - C_g)H_\varepsilon(\varphi) \tag{33}$$

The subscripts m and g represent the melt phase and the gas phase in the cavity respectively. The subscripts s, f and l represent the solid, mush and liquid states

of the polymer melt respectively. Thus, symbol $T_{m,s}$ is the solid state temperature threshold for the melt phase. The meanings of other symbols are similar. Note that the gas phase will always the gas state in the cavity, so the same value of T_g is used in Eqs. (28) and (29), and the same value of C_g is used in Eqs. (31)-(33). Thus, these expressions will be the relationship between H and T for the melt when $H_\varepsilon(\varphi) = 1$, while for the air in the cavity when $H_\varepsilon(\varphi) = 0$.

Introduce the Kirchhoff Temperature $T_{kir} = \Gamma(H)H + S(H)$, the expression of the Enthalpy model can be given as follows.

$$Pe\left(\frac{\partial \rho H}{\partial t} + \nabla \cdot (\rho \mathbf{u} H)\right) = \nabla^2(\Gamma(H)H + S(H)) + Br(\sigma : \mathbf{D}) \tag{34}$$

In which,

$$\Gamma(H) = \begin{cases} \frac{k_s}{C_s}, & H \leq 0 \\ \frac{k_f(T_l - T_s)}{L_H + C_f(T_l - T_s)}, & 0 < H < L_H + C_f(T_l - T_s) \\ \frac{k_l}{C_l} & H \geq L_H + C_{p,f}(T_l - T_s) \end{cases} \tag{35}$$

$$S(H) = \begin{cases} 0, & H \leq 0 \\ 0, & H < L_H + C_f(T_l - T_s) \\ -k_l \frac{L_H + (C_f - C_l)(T_l - T_s)}{C_l}, & H \geq L_H + C_f(T_l - T_s) \end{cases} \tag{36}$$

and

$$k_s = k_g + (k_{m,s} - k_g)H_\varepsilon(\varphi) \tag{37}$$

$$k_f = k_g + (k_{m,f} - k_g)H_\varepsilon(\varphi) \tag{38}$$

$$k_l = k_g + (k_{m,l} - k_g)H_\varepsilon(\varphi) \tag{39}$$

2.4 Cross-WLF model

The Cross-WLF model, which is the most appropriate model for studying both filling and packing phases, has been chosen to assess the total viscosity η of the polymer melt and adjust better the temperature and pressure sensitivities of zero-shear-rate viscosity [Boronat, Segui, Peydro, and Reig (2009)]. It specifies that

$$\eta_l(T, \dot{\gamma}, p) = \frac{\eta_0(T, p)}{1 + (\eta_0 \dot{\gamma}/\tau^*)^{1-n}}, \tag{40}$$

where $\eta_0(T, p)$ is the melt viscosity under zero-shear-rate condition, τ^* is a constant that gives the shear stress rate from which the pseudoplastic behavior of the melt starts. n is the non-Newtonian index chosen so that the pseudoplastic behavior gradient is $1 - n$, $\dot{\gamma}$ is the shear rate.

The WLF expression determines the viscosity of the melt under zero-shear-rate conditions

$$\eta_0 = D_1 \exp((-A_1(T-T^*))/(A_2+(T-T^*)) \tag{41}$$

where $T^* = D_2 + D_3 p$, $A_2 = \tilde{A}_2 + D_3 p$, the constant A_1 is the temperature dependence of melt glass transition temperature under zero-shear-rate conditions. The constant D_1 is the melt viscosity, under zero-shear-rate conditions, at melt glass transition temperature and at atmospheric pressure. T^* is the glass transition temperature of the melt, depending on the pressure. D_2 is the glass transition temperature. D_3 is the variation of the glass transition temperature of the melt with pressure. The value of parameter $\tilde{A}_2$ depends on the type of polymer melt that has been considered.

Equations (1), (4), (20), (21), (34), (40) and (41) compose the model for the non-isothermal non-Newtonian fluid mold filling process with phase change.

3 Numerical methods

3.1 Numerical methods for governing equations of the non-Newtonian flow

The finite volume SIMPLE method on a non-staggered grid is used to solve the governing equations (20), (21) and (34). A non-staggered grid arrangement, which stores all the variables at the same physical location and employs only one set of control volumes, is shown in Fig. 1, where the dashed lines are the faces of control volumes or cells and the intersection points of the solid lines are the nodes on which all the physical quantities are located [Tao (2001)]

3.1.1 Continuity equation

The continuity equation (20) can be discretized into the following form by integrating over the control volume.

$$((\rho u)_e - (\rho u)_w)\Delta y + ((\rho \upsilon)_n - (\rho \upsilon)_s)\Delta x = 0 \tag{42}$$

3.1.2 Momentum equations

The discretization of the momentum equation (21) can be written in the following form for a generalized quantity ψ.

$$a_P \psi_P = a_E \psi_E + a_W \psi_W + a_N \psi_N + a_S \psi_S + S_\psi, \tag{43}$$

where S_ψ is the source term in the momentum equation. The coefficients a_E, a_W, a_N, a_S, a_P can be expressed as the combination of the convection term and the

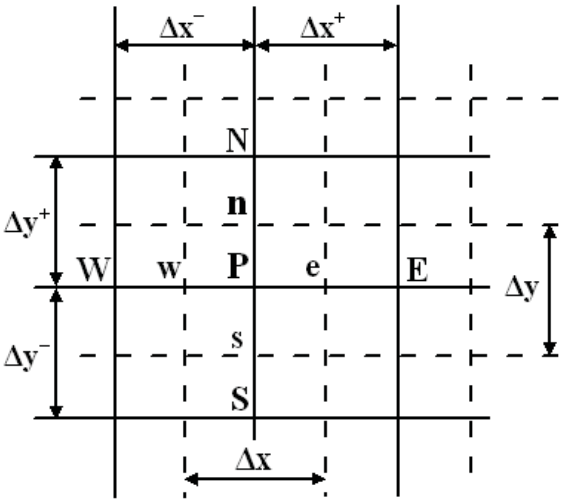

Figure 1: Sketch map of the non-staggered meshes

diffusion term, i.e.

$$\begin{aligned} &a_E = D_e A(|P_e|) + \max(-F_e, 0), \quad a_W = D_W A(|P_w|) + \max(F_W, 0), \\ &a_N = D_n A(|P_n|) + \max(-F_n, 0), \quad a_S = D_S A(|P_s|) + \max(F_S, 0), \\ &a_P = a_E + a_W + a_N + a_S + \Delta x \Delta y \rho / \Delta t. \end{aligned} \tag{44}$$

Here P_e, P_w, P_n, P_s are the Peclet numbers on the cell faces, F_e, F_w, F_n, F_s are the cell faces flux, and D_e, D_w, D_n, D_s denote diffuse derivatives on cell faces. The form of $A(|P_e|)$ can be different under different discretization schemes for the convection term. For example, $A(|P_\Delta|)$ equals 1 for the upwind scheme while $1 - 0.5|P_\Delta|$ is used for a central scheme. We take $A(|P_e|) = 1$ in this paper. All the coefficients are formulated as follows.

$$\begin{aligned} &F_e = (\rho u)_e \Delta y, \quad D_e = \tfrac{\eta_e \Delta y}{(x_E - x_P) Re}, \quad P_e = \tfrac{F_e}{D_e} \\ &F_w = (\rho u)_w \Delta y, \quad D_w = \tfrac{\eta_w \Delta y}{(x_P - x_W) Re}, \quad P_w = \tfrac{F_w}{D_w} \\ &F_n = (\rho \upsilon)_n \Delta x, \quad D_n = \tfrac{\eta_n \Delta x}{(y_N - y_P) Re}, \quad P_n = \tfrac{F_n}{D_n} \\ &F_s = (\rho \upsilon)_s \Delta x, \quad D_s = \tfrac{\eta_s \Delta x}{(y_P - y_S) Re}, \quad P_s = \tfrac{F_s}{D_s} \end{aligned} \tag{45}$$

3.1.3 Energy equations

The Energy equation can be as

$$a_P T_P = a_E T_E + a_W T_W + a_N T_N + a_S T_S + S_T \tag{46}$$

Similarly, the coefficients a_E, a_W, a_N, a_S, a_P can be expressed as the combination of the convection term and the diffusion term, i.e.

$$\begin{aligned} &a_E = D_e A(|P_e|) + \max(-F_e, 0), && a_W = D_w A(|P_w|) + \max(F_w, 0), \\ &a_N = D_n A(|P_n|) + \max(-F_n, 0), && a_S = D_s A(|P_s|) + \max(F_s, 0), \\ &a_P = a_E + a_W + a_N + a_S + Pe\Delta x\Delta y\rho/\Delta t \end{aligned} \tag{47}$$

$$\begin{aligned} &F_e = Pe(\rho u)_e \Delta y, && D_e = \Gamma(H)\tfrac{\Delta y}{(x_E - x_P)}, && P_e = \tfrac{F_e}{D_e}, \\ &F_w = Pe(\rho u)_w \Delta y, && D_w = \Gamma(H)\tfrac{\Delta y}{(x_P - x_W)}, && P_w = \tfrac{F_w}{D_w}, \\ &F_n = Pe(\rho u)_n \Delta y, && D_n = \Gamma(H)\tfrac{\Delta x}{(y_N - y_P)}, && P_n = \tfrac{F_n}{D_n}, \\ &F_s = Pe(\rho u)_s \Delta y, && D_s = \Gamma(H)\tfrac{\Delta x}{(y_P - y_S)}, && P_s = \tfrac{F_s}{D_s}. \end{aligned} \tag{48}$$

3.2 Numerical methods for level set and the reinitialization equation

The level set evolution equation (1) and the reinitialization equation (4) are solved by the finite difference method on a rectangular grid. The spatial derivatives are discretized by the 5th-order Weighted Essentially Non-Oscillatory (WENO) scheme [Jiang and Peng (2000); Osher and Shu (1991)] and the temporal derivatives are discretized by the 3rd-order Total Variation Diminishing Runge-Kutta (TVD-R-K) scheme [Shu and Osher (1989)].

3.2.1 WENO scheme

Define $\varphi_{i,j} = \varphi(x_i, y_j)$, $\Delta_x^+ \varphi_{i,j} = \varphi_{i+1,j} - \varphi_{i,j}$, $\Delta_y^+ \varphi_{i,j} = \varphi_{i,j+1} - \varphi_{i,j}$, then the 5-order WENO scheme for the numerical approximations of the partial derivatives φ_x, φ_y is

$$\begin{aligned} \varphi_{x,i,j}^{\pm} =& \frac{1}{12}\left(-\frac{\Delta_x^+\varphi_{i-2,j}}{\Delta x} + 7\frac{\Delta_x^+\varphi_{i-1,j}}{\Delta x} + 7\frac{\Delta_x^+\varphi_{i,j}}{\Delta x} - \frac{\Delta_x^+\varphi_{i+1,j}}{\Delta x}\right) \\ &\pm \Psi^{WENO}\left(\frac{\Delta_x^-\Delta_x^+\varphi_{i\pm2,j}}{\Delta x}, \frac{\Delta_x^-\Delta_x^+\varphi_{i\pm1,j}}{\Delta x}, \frac{\Delta_x^-\Delta_x^+\varphi_{i,j}}{\Delta x}, \frac{\Delta_x^-\Delta_x^+\varphi_{i\mp1,j}}{\Delta x}\right), \end{aligned} \tag{49a}$$

$$\begin{aligned} \varphi_{y,i,j}^{\pm} =& \frac{1}{12}\left(-\frac{\Delta_y^+\varphi_{i,j-2}}{\Delta y} + 7\frac{\Delta_y^+\varphi_{i,j-1}}{\Delta y} + 7\frac{\Delta_y^+\varphi_{i,j}}{\Delta y} - \frac{\Delta_y^+\varphi_{i,j+1}}{\Delta y}\right) \\ &\pm \Psi^{WENO}\left(\frac{\Delta_y^-\Delta_y^+\varphi_{i,j\pm2}}{\Delta y}, \frac{\Delta_y^-\Delta_y^+\varphi_{i,j\pm1}}{\Delta y}, \frac{\Delta_y^-\Delta_y^+\varphi_{i,j}}{\Delta y}, \frac{\Delta_y^-\Delta_y^+\varphi_{i,j\mp1}}{\Delta y}\right), \end{aligned} \tag{49b}$$

where the function Ψ^{WENO} is expressed as

$$\Psi^{WENO}(a,b,c,d) = -\frac{1}{3}\omega_0(a-2b+c) + \frac{1}{6}(\omega_2 - \frac{1}{2})(b-2c+d). \tag{50}$$

The expressions for ω_0, ω_2 are

$$\omega_0 = \frac{\alpha_0}{\alpha_0+\alpha_1+\alpha_2}, \quad \omega_2 = \frac{\alpha_2}{\alpha_0+\alpha_1+\alpha_2}, \tag{51}$$

where

$$\alpha_0 = \frac{1}{(\varepsilon'+S_0)^2}, \alpha_1 = \frac{6}{(\varepsilon'+S_1)^2}, \alpha_2 = \frac{3}{(\varepsilon'+S_2)^2}, \tag{52}$$

$$\begin{aligned} S_0 &= 13(a-b)^2+3(a-3b)^2, \\ S_1 &= 13(b-c)^2+3(b+c)^2, \\ S_2 &= 13(c-d)^2+3(3c-d)^2, \end{aligned} \tag{53}$$

and ε' is a very small number used for avoiding division by zero.

3.2.2 TVD-R-K scheme

The 3-order TVD-R-K scheme can be expressed as

$$\begin{aligned} \varphi^{(1)} &= \varphi^{(0)} + \Delta t L(\varphi^{(0)}), \\ \varphi^{(2)} &= \varphi^{(1)} + \frac{\Delta t}{4}(-3L(\varphi^{(0)}) + L(\varphi^{(1)})), \\ \varphi^{(3)} &= \varphi^{(2)} + \frac{\Delta t}{12}(-L(\varphi^{(0)}) - L(\varphi^{(1)}) + 8L(\varphi^{(2)})), \end{aligned} \tag{54}$$

where $\varphi^{(0)} = \varphi^n$, $\varphi^{(3)} = \varphi^{n+1}$, and $L(\varphi) = -u\varphi_x - \upsilon\varphi_y$ for the level set function, while $L(\varphi) = \text{sign}(\varphi_0)(1-|\nabla\varphi|)$ for the reinitialization equation.

3.3 Boundary conditions and determination of time step

Proper boundary conditions must be posed on the solid walls of the cavity. We used the boundary conditions proposed by Yang, Ouyang, Liu, and Li (2010) for two-phase flow. When Eqs. (20)-(21) are solved, no-slip boundary conditions are used for the velocities, that is, $\mathbf{u} = 0$. As for the pressure boundary conditions, for the air in the cavity, we use $p = 0$, while for the melt in the cavity, no-penetration boundary conditions are used, i.e. $\partial p/\partial \mathbf{n} = 0$.

The time step Δt is determined by restrictions due to the CFL condition and viscosity [Sussman, Fatemi, Smereka, and Osher (1998)]. Define

$$\Delta t_c = \min\left(\frac{\Delta x}{|\mathbf{u}|}\right)$$

$$\text{and } \Delta t_\eta = \min\left(\frac{3}{14}\frac{\rho Re \Delta x^2}{\eta}\right),$$

then the overall restriction on the time step is $\Delta t = \frac{1}{2}\min(\Delta t_c, \Delta t_\eta)$.

4 Numerical test for benchmark problems

4.1 Non-isothermal Flow through a 4:1 planar contraction

The benchmark problem of non-isothermal flow through a 4:1 planar contraction is considered, the isothermal case of which has been verified by Yang, Ouyang, Li, Zhao, and Liu (2010). Fluid passes from one channel into another of smaller cross-sectional width and in the process generates a complex flow exhibiting regions of strong shearing near the walls and planar extension along the centerline. The lengths of upstream and downstream are $10L$ and $20L$, respectively. The velocities at the inlet are given as $u = 3/8(1.0 - y^2/16)$ and $\upsilon = 0$. At the outlet Neumann boundary conditions are given under the assumption of fully-developed conditions. No-slip boundary conditions are imposed along the stationary walls. Symmetry boundary conditions are imposed along the central line. The temperature on the solid walls is given as $273K$, while that at the entrance is $323K$.

Figure 2 gives the temperature distributions at different *Pe* numbers. We see from Fig. 2(a) that when *Pe* is very small, there will be a district with special high temperature near the contraction part of the computational area. This has two causes. On one hand, since *Pe* number is very small, the effect of heat convection can almost be ignored compared with that of heat dissipation. On the other hand, the velocities vary sharply near the contraction district so that the heat dissipation in this area is much larger than that in other areas and the temperature in this area increases as a result. Things become different as *Pe* number increases, which means the effect of heat convection has the dominant position gradually. The high temperature can be transported deep into the whole computational area by velocities and the 'local hot point' caused by heat dissipation disappears gradually.

4.2 Zalesak's Sphere problem

We now use a slotted sphere to test our scheme for level set equations. The sphere has a radius of 15. The domain size is $100 \times 100 \times 100$. The slot has a width of 6 and a depth of 24. The sphere is initially placed at (50,75,50) and undergoes a rotation about the point (50,50,50) in the plane $z = 50$ [Ville, Silva, and Coupez (2010); Yang, Ouyang, Li, Zhao, and Liu (2010)]. We initialize $\mathbf{u}$ as follows

$$u_0 = (\pi/314)(50 - y), \upsilon_0 = (\pi/314)(x - 50), w_0 = 0.$$

φ_0 is set to be the signed distance from object. We compute for $t = 0 \sim 628$. The time step is set to be equal to Δx. The results at different time are shown in Fig. 3. The solution has lost only 4.6% of the initial volume after one revolution.

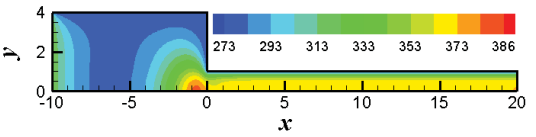

(a). $Pe = 1.0$

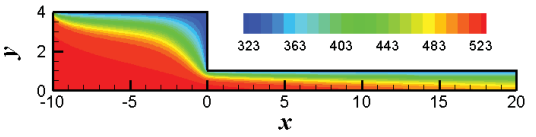

(b). *Pe*=100. 0

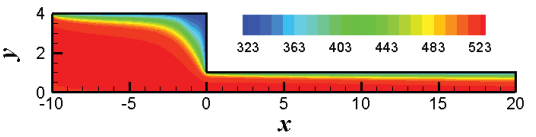

(c). *Pe*=1000. 0

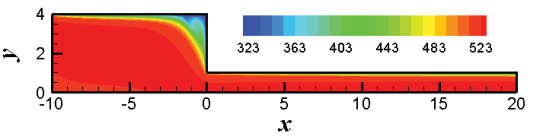

(d). *Pe*=10000. 0

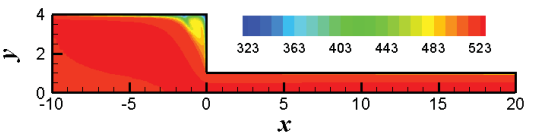

(e). *Pe*=100000. 0

Figure 2: Temperature distributions at different Peclet numbers

$t = 0$ $t = 157$ $t = 314$ $t = 471$ $t = 628$

Figure 3: Zalesak's sphere problem

5 Numerical simulation and results

5.1 Computational domain and parameters setting

A sketch of the injection mold is shown in Fig. 4(a), in which the shaded area, i.e. the vertical middle plane of the mold, is the computational domain (Fig. 4(b)). Suppose the length and width of the computational area are 10.0 and 1.0 respectively The initial interface is set to be a semicircle with a radius of 0.5 which is shown in Fig. 4(b).

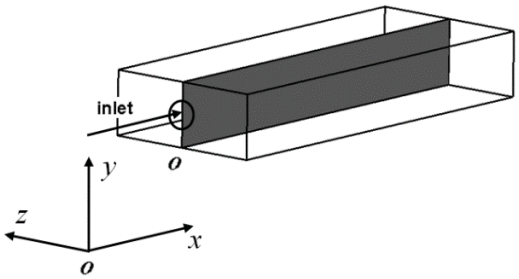

(a) Sketch map and the computational area (shaded area) of the mold

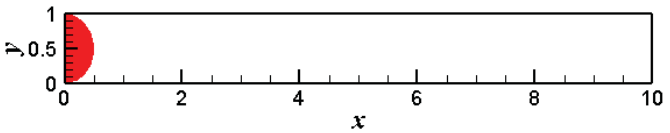

(b) Computational area with initial interface (shaded)

Figure 4: Mold and computational area

High density polyethylene (HDPE) is used as the polymer melt, the material properties parameters and thermal property parameters of which are given in Table 1 and Table 2 respectively. The solidification temperature of HDPE is $377K$. The thermal property parameters of the air in the cavity are given in Table 3. It is worth mentioning that the parameters values in Table 3 guarantee that the air is always in the gaseous state.

Table 1: Material properties of HDPE [Liu (2003)]

n	τ^*/Pa	$D_1/Pa\cdot S$	D_2/K	$D_3/(Pa/K)$	A_1	$\tilde{A}_2/K$
0.3794	105985	5.769×10^{13}	233.15	0.1	32.344	51.6

Table 2: Thermal property parameters of HDPE [Liu (2003)]

$k_{m,s}$ (W/mK)	$k_{m,l}$ (W/mK)	$C_{m,s}$ (J/kgK)	$C_{m,l}$ (J/kgK)	L_m (J/kg)	$T_{m,s}$ (K)	$T_{m,l}$ (K)
0.316	0.238	2042.0	2990.0	1.8×10^5	377.0	381.0

Table 3: Thermal property parameters of air in the cavity [Liu (2003)]

k_g (W/mK)	C_g (J/kgK)	L_g (J/kg)	T_g (K)
0.023	1000.0	2260.0	0.0

5.2 Interface evolution

Figure 5 shows the interface evolution at different times in the cavity, when the temperatures of the solid walls and the melt are set to be $T_{wall} = 343K$ and $T_{melt} = 533K$ respectively, and the injection velocity is set to be $u = -20\times(y-0.5)^2+5.0$, $y\in[0,1]$. Since the velocity is not very high, the melt will extend as arcs instead of a jet, in accordance with the experimental result given in Fig. 5(b).

5.3 Pressure

The pressure contours at various time are presented in Fig. 6, from which we see that the pressure values decrease from the inlet to the end of the cavity, and with the maximum pressure value always at the inlet.

5.4 Fountain flow

Figure 7 clearly shows the fountain flow effect at $t = 1200\Delta t$, i.e., polymer material approaches the flow front from the center and diverts towards the wall.

5.5 Temperature

The temperature contours at selected times are given in Fig. 8.

Figure 9 shows the distribution of the temperatures which are below the solidification temperature when the cavity is filled with melt. Both the temperatures of the melt and the solid wall are high enough that no “frozen skin” layer is found in this case.

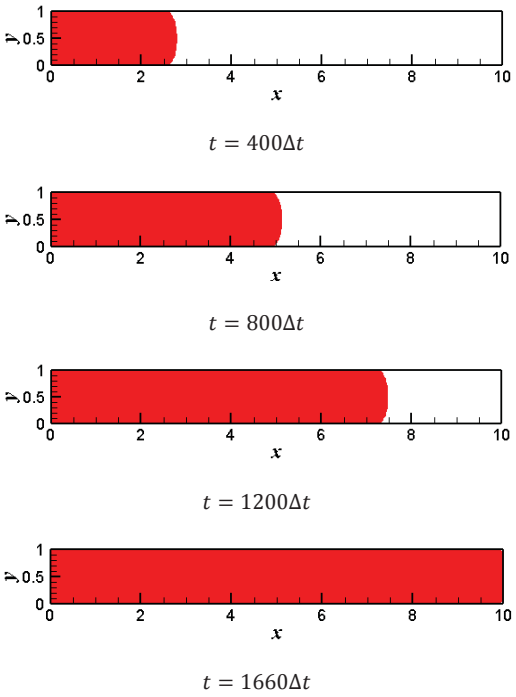

(a) Numerical results(shaded area is the melt)

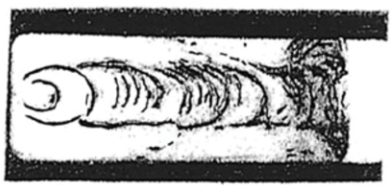

(b) Experimental result [Han (2007)].

Figure 5: Interface evolution with $T_{wall} = 343K$ and $T_{melt} = 533K$

5.6 Discussion about the "frozen skin" layers at different cases

In order to discuss the "frozen skin" layer, we given different simulation results at different solid wall and melt temperatures.

Firstly, an extreme case is given, in which we set $T_{wall} = 283K$ and $T_{melt} = 433K$. The temperature distribution when the cavity is filled with melt is given in Fig. 10, from which we see that the temperatures near the solid walls are very low. Temperature values decrease from the inlet to the end of the cavity. Figure 11 shows

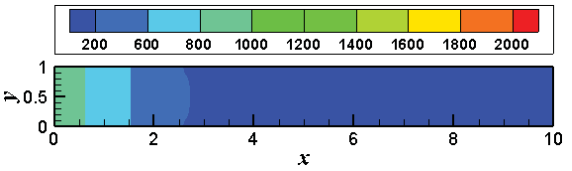

$t = 400\Delta t$

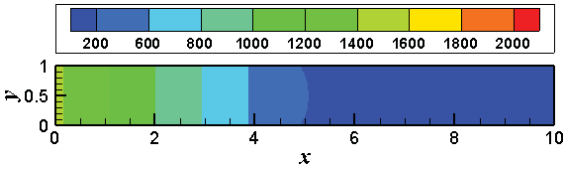

$t = 800\Delta t$

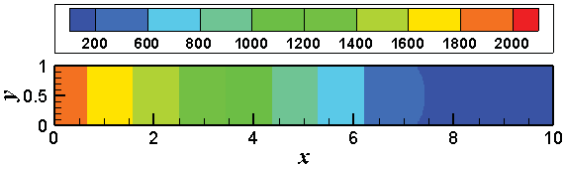

$t = 1200\Delta t$

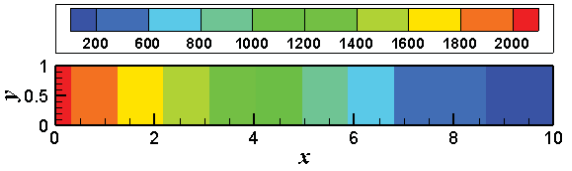

$t = 1660\Delta t$

Figure 6: Pressure contours with $T_{wall} = 343K$ and $T_{melt} = 533K$

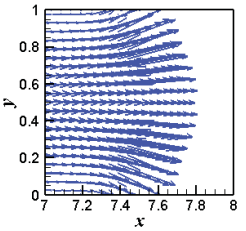

Figure 7: Fountain flow effect at $t = 1200\Delta t$

the “frozen skin” layer distribution, which a very thick “frozen skin” layer can be found near the solid walls of the cavity, especially at the end of the cavity.

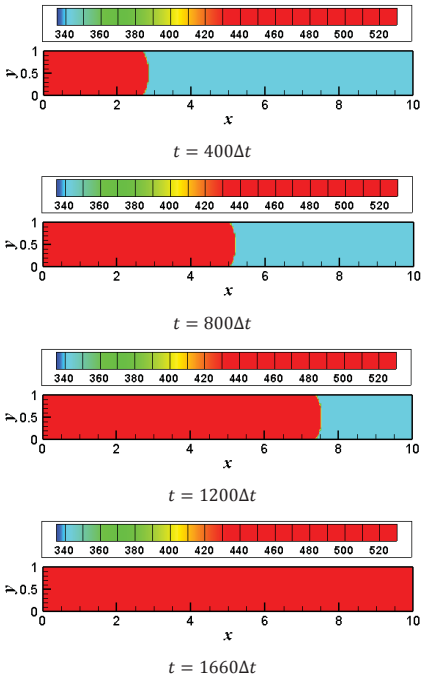

Figure 8: Temperature contours with $T_{wall} = 343K$ and $T_{melt} = 533K$

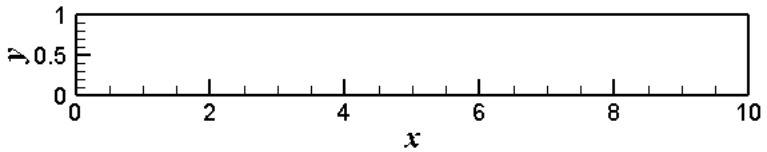

Figure 9: Distribution of the temperatures which are below the solidification temperature

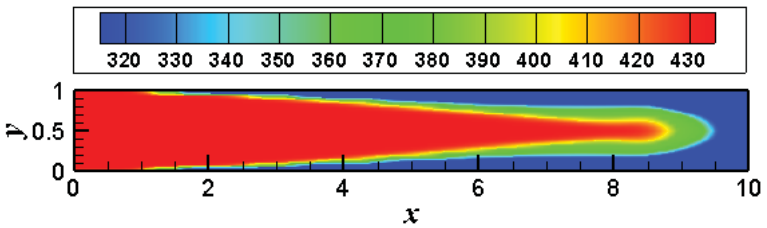

Figure 10: Temperature distribution with $T_{wall} = 283K$ and $T_{melt} = 433K$

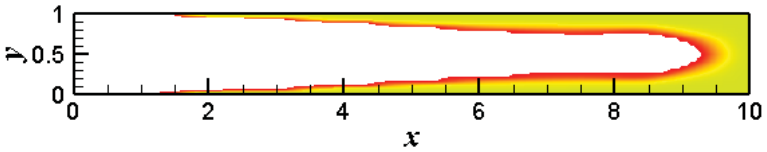

Figure 11: "frozen skin" layer with $T_{wall} = 283K$ and $T_{melt} = 433K$

As described by Kumar, Ghoshdastida, and Muju (2002), the "frozen skin" layer is not desirable because it contributes to the "molded in" strains in the molded article. The "frozen skin" layer can be effectively reduced or eliminated by higher injection pressure (resulting in higher flow rate), higher melt temperature, and to a lesser but appreciable degree by increasing mold temperature. We now test the influence of T_{wall}, T_{melt} and the injection velocity on the "frozen skin" layer.

5.6.1 Influence of the solid wall temperature T_{wall} on "frozen skin" layer

We keep the melt temperature at $T_{melt} = 433K$ and increase the temperature on the solid walls of the cavity to $T_{wall} = 320K$. The distributions of temperature and "frozen skin" layer after the cavity is filled with melt are given in Figs. 12 and 13 respectively.

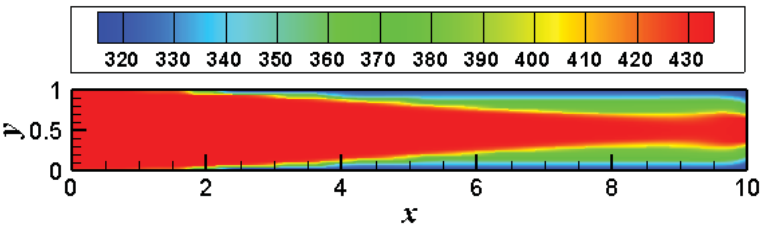

Figure 12: Temperature distribution with $T_{wall} = 320K$ and $T_{melt} = 433K$

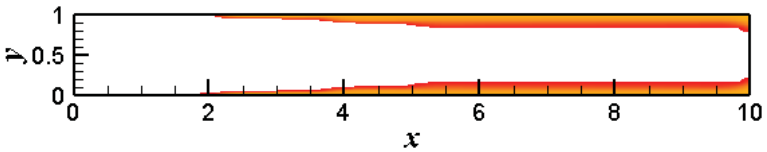

Figure 13: "frozen skin" layer with $T_{wall} = 320K$ and $T_{melt} = 433K$

The case when $T_{wall} = 321K$ and $T_{melt} = 433K$ is given by Fig. 14 and Fig. 15. A thinner "frozen skin" layer can be found.

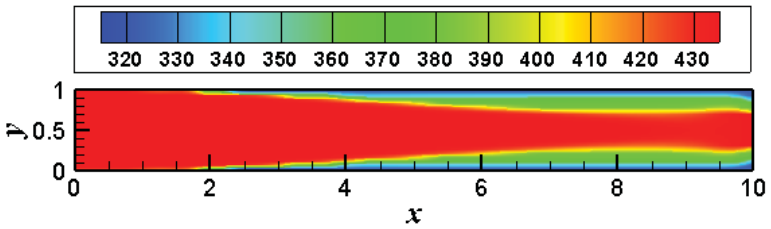

Figure 14: Temperature distribution with $T_{wall} = 321K$ and $T_{melt} = 433K$

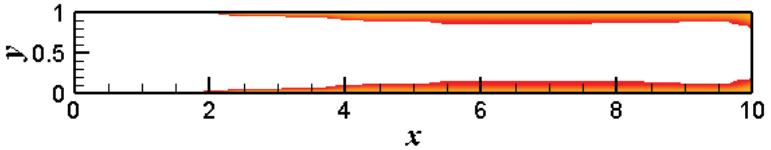

Figure 15: "frozen skin" layer with $T_{wall} = 321K$ and $T_{melt} = 433K$

When we set $T_{wall} = 323K$ the "frozen skin" layer will completely disappear, which is shown in Fig. 16 and Fig. 17.

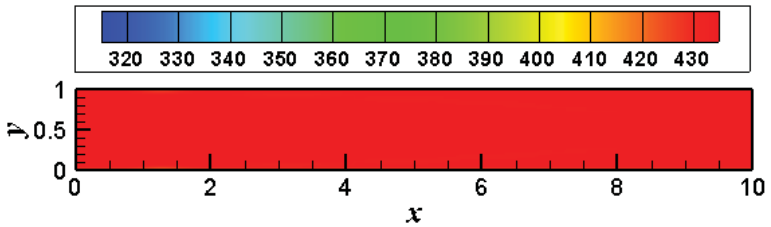

Figure 16: Temperature distribution with $T_{wall} = 323K$ and $T_{melt} = 433K$

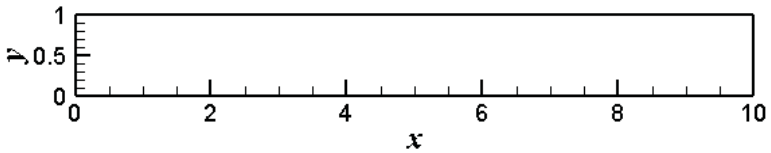

Figure 17: "frozen skin" layer with $T_{wall} = 323K$ and $T_{melt} = 433K$

All the cases in this section verify that "frozen skin" layer can be eliminated by increasing the temperature of the cavity.

5.6.2 Influence of the solid wall temperature T_{melt} on "frozen skin" layer

We now change the value of $T_{melt} = 533K$, while T_{wall} remains $283K$. The results are given in Fig. 18 and Fig. 19, in which no "frozen skin" layer can be found. This case verifies that increasing the temperature of the melt can eliminate the "frozen skin" layer effectively.

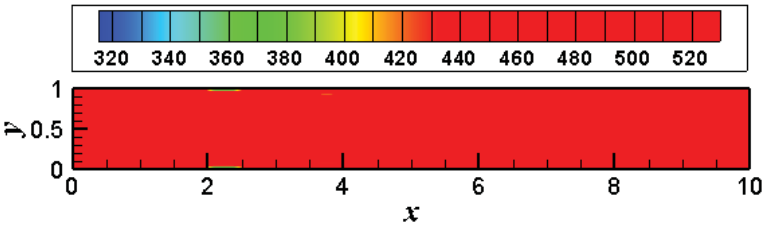

Figure 18: Temperature distribution with $T_{wall} = 283K$ and $T_{melt} = 533K$

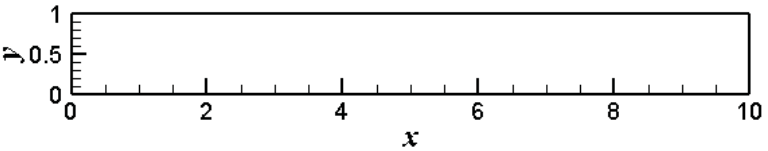

Figure 19: "frozen skin" layer with $T_{wall} = 283K$ and $T_{melt} = 533K$

5.6.3 Influence of injection velocity on "frozen skin" layer

In all the above cases, the injection velocity is set to be $u = -20 \times (y-0.5)^2 + 5.0$, $y \in [0,1]$. Now we change the injection velocity to be $u = -4 \times (y-0.5)^2 + 1.0$, $y \in [0,1]$, which is slower than that in the above cases. The temperatures are set to be $T_{wall} = 321K$ and $T_{melt} = 433K$.

The distributions of temperature and "frozen skin" layer after the cavity is filled with melt are given in Figs. 20 and 21 respectively. A local comparison of the "frozen skin" layers between the two injection velocities is shown in Fig. 22, from which we see that a slower injection velocity leads to a thicker "frozen skin" layer.

6 Conclusion

In this paper, a 2D non-isothermal injection molding process for a non-Newtonian viscous pseudoplastic fluid is simulated with phase change. A conservative level set method is used to capture the evolution of the interface and the finite volume

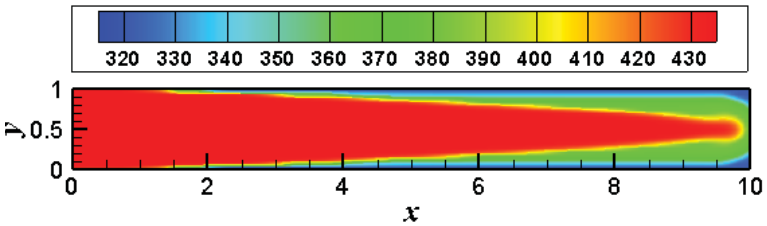

Figure 20: Temperature distribution with $T_{wall} = 321K$ and $T_{melt} = 433K$ and $u = -4 \times (y-0.5)^2 + 1.0$, $y \in [0,1]$

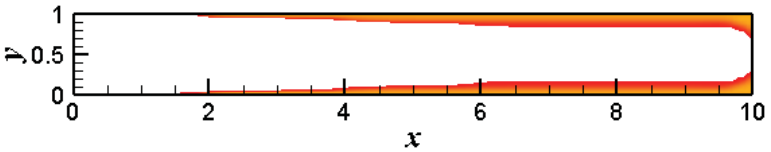

Figure 21: "frozen skin" layer with $T_{wall} = 321K$ and $T_{melt} = 433K$ and $u = -4 \times (y-0.5)^2 + 1.0$, $y \in [0,1]$

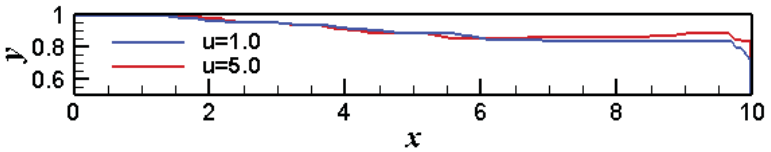

Figure 22: A local comparison of the "frozen skin" layers between the two injection velocities

method is used to get the information of the flow field. A modified Enthalpy model for two-phase flow is proposed to describe the phase change in the mold filling process. The information including the melt interface and the physical quantities such as temperature, pressure and velocity are all obtained.

The decrease of temperature near cavity walls leads to high viscosity values and the reduction of the velocities in this zone, where a "frozen skin" layer will appear. The influences of the solid wall temperature, the melt temperature and injection velocity on "frozen skin" layer are discussed in detail. The "frozen skin" layer can be effectively reduced or eliminated by higher injection pressure (resulting in higher flow rate), higher melt temperature, and to a lesser but appreciable degree by increasing mold temperature.

The results of this work are helpful for the mold design and the model and proposed

method can be extended to the 3D case.

Acknowledgment

All the authors would like to acknowledge the National Natural Science Foundation of Shanxi Province (2012011019-2, 2011011021-3), the Graduate Outstanding Innovation Project of Shanxi Province (20133114) and research funding of Taiyuan University of Science and Technology (20112011).

References

Au, C. K. (2005): A geometric approach for injection mould filling simulation. *International Journal of Machine Tools & Manufacture*, vol. 45, no. 1, pp. 115–124.

Ayad, R.; Rigolot, A. (2002): The vof-g/fev model for tracking a polymer-air interface in the injection moulding process. *Journal of Mechanical Design*, vol. 24, no. 4, pp. 813–821.

Bonito, A.; Picasso, M.; Laso, M. (2006): Numerical simulation of 3d viscoelastic flows with free surfaces. *Journal of Computational Physics*, vol. 215, no. 2, pp. 691–716.

Boronat, T.; Segui, V. J.; Peydro, M. A.; Reig, M. J. (2009): Influence of temperature and shear rate on the rheology and processability of reprocessed abs in injection molding process. *Journal of Materials Processing Technology*, vol. 209, no. 5, pp. 2735–2745.

Cahn, J. W.; Hilliard, J. E. (1958): Free energy of a nonuniform system. i: interfacial free energy. *The Journal of Chemical Physics*, vol. 28, no. 2, pp. 1015–1031.

Caldwell, J.; Date, A. W. (2003): Implicit enthalpy formulation of phase-change problems on unstructured grid. *Communications in Numerical Methods in Engineering*, vol. 19, no. 11, pp. 865–875.

Cao, Y.; Faghri, A.; Chang, W. S. (1989): A numerical analysis of stefan problems for generalized multi-dimensional phase-change structures using the enthalpy transforming model. *International Journal of Heat and Mass Transfer*, vol. 32, no. 7, pp. 1289–1298.

Carslaw, H. S.; Jaeger, J. S. (1959): *Conduction of Heat in Solids*. Oxford University Press.

Chang, R. Y.; Yang, W. H. (2001): Numerical simulation of mold filling in injection molding using a three-dimensional finite volume approach. *International Journal for Numerical Methods in Fluids*, vol. 27, no. 2, pp. 125–148.

Chiang, H. H.; Hieber, C. A.; Wang, K. K. (1991): A unified simulation of the filling and postfilling stages in injection-molding. 1: Formulation. *Polymer Engineering and Science*, vol. 31, no. 2, pp. 116–124.

Crowley, A. B. (1978): Numerical solution of stefan problems. *International Journal of Heat and Mass Transfer*, vol. 21, no. 2, pp. 215–219.

Geng, T.; Li, D. Q.; Zhou, H. M. (2006): Three-dimensional finite element method for the filling simulation of injection molding. *Engineering with Computers*, vol. 21, no. 4, pp. 289–295.

Han, C. D. (2007): *Rheology and Processing of Polymeric Materials*. Oxford University Press.

Hetu, J. F.; Gao, D. M.; Garcia-Rejon, A.; Salloum, G. (1998): 3d finite element method for the simulation of the filling stage in injection molding. *Polymer Engineering and Science*, vol. 38, no. 2, pp. 223–236.

Holm, E. J.; Langtangen, H. P. (1999): A unified finite element model for the injection molding process. *Computer Methods in Applied Mechanics and Engineering*, vol. 178, no. 3-4, pp. 413–429.

Jiang, G. S.; Peng, D. P. (2000): Weighted eno schemes for hamilton-jacobi equations. *Siam Journal on Scientific Computing*, vol. 21, no. 6, pp. 2126–2143.

Kabanemi, K. K.; Vaillancourt, H.; Wang, H.; Salloum, G. (1998): Residual stresses, shrinkage, and warpage of complex injection molded products: numerical simulation and experimental validation. *Polymer Engineering and Science*, vol. 38, no. 1, pp. 21–37.

Khayat, R. E.; Elsin, W.; Kim, K. (2000): An adaptive boundary element approach to transient free surface flow as applied to injection molding. *International Journal for Numerical Methods in Fluids*, vol. 33, no. 6, pp. 847–868.

Khor, C. Y.; Ariff, Z. M.; Ani, F. C.; Mujeebu, M. A.; Abdullah, M. K.; Abdullah, M. Z.; Joseph, M. A. (2010): Three-dimensional numerical and experimental investigations on polymer rheology in meso-scale injection molding. *International Communications in Heat and Mass Transfer*, vol. 37, no. 2, pp. 131–139.

Kim, M. S.; Park, J. S.; Lee, W. I. (2003): A new vof-based numerical scheme for the simulation of fluid flow with free surface. part ii: application to the cavity filling and sloshing problems. *International Journal for Numerical Methods in Fluids*, vol. 42, no. 7, pp. 791–812.

Kim, S.; Kim, M. C.; Chun, W. G. (2001): A fixed grid finite control volume model for the phase change heat conduction problems with a single-point predictor-corrector algorithm. *Korean Journal of Chemical Engineering*, vol. 18, no. 1, pp. 40–45.

Kim, S. W.; Turng, L. S. (2006): Three-dimensional numerical simulation of injection molding filling of optical lens and multiscale geometry using finite element method. *Polymer Engineering and Science*, vol. 46, no. 9, pp. 1263–1274.

Krabbenhoft, K.; Damkilde, L.; Nazem, M. (2007): An implicit mixed enthalpy-temperature method for phase-change problems. *International Journal of Heat and Mass Transfer*, vol. 43, no. 3, pp. 233–241.

Kumar, A.; Ghoshdastida, P. S.; Muju, M. K. (2002): Computer simulation of transport processes during injection mold-filling and optimization of the molding conditions. *Journal of Materials Processing Technology*, vol. 120, no. 1-3, pp. 428–449.

Li, Q.; Ouyang, J.; Li, X. J.; Wu, G. R.; Yang, B. X. (2011): Numerical simulation of gas-assisted injection molding process for a door handle. *Computer Modeling in Engineering and Sciences*, vol. 74, no. 4, pp. 247–267.

Liu, C. T. (2003): *Simulation-based studies on processing optimization and part performance in injection molding*. Zhengzhou University Press.

Luoma, J. A.; Voller, V. R. (2000): An explicit scheme for tracking the filling front during polymer mold filling. *Applied Mathematical Modeling*, vol. 24, no. 8-9, pp. 575–590.

Osher, S.; Fedkiw, R. P. (2001): Level set methods: An overview and some recent results. *Journal of Computational Physics*, vol. 169, no. 2, pp. 463–502.

Osher, S.; Shu, C. W. (1991): High-order essentially non-oscillatory schemes for hamilton- jacobi equations. *SIAM Journal on Numerical Analysis*, vol. 28, pp. 907–922.

Pichelin, E.; Coupez, T. (1998): Finite element solution of the 3d mold filling problem for viscous incompressible fluid. *Computer Methods in Applied Mechanics and Engineering*, vol. 163, no. 1-4, pp. 359–371.

Rubinstein, L. I. (1994): *The Stefan Problem*. Providence Press.

Shu, C. W.; Osher, S. (1989): Efficient implementation of essentially non-oscillatory shock-capturing schemes, ii. *Journal of Computational Physics*, vol. 83, no. 1, pp. 32–78.

Smith, D. E.; Tortorelli, D. A.; Tucker, C. L. (1998): Analysis and sensitivity analysis for polymer injection and compression molding. *Computer Methods in Applied Mechanics and Engineering*, vol. 167, no. 3-4, pp. 325–344.

Soukane, S.; Trochu, F. (2006): Application of the level set method to the simulation of resin transfer molding. *Composites Science and Technology*, vol. 66, no. 7-8, pp. 1067–1080.

Sussman, M.; Fatemi, E.; Smereka, P.; Osher, S. (1998): An improved level set method of incompressible two-phase flows. *Computers and Fluid*, vol. 27, pp. 663–680.

Tao, W. Q. (2001): *Numerical Heat Transfer*. Xi'an Jiaotong University Press.

Ville, L.; Silva, L.; Coupez, T. (2010): Convected level set method for the numerical simulation of fluid buckling. *International Journal for Numerical Methods in Fluids*, vol. 66, no. 3, pp. 324–344.

Wang, J.; Andres, E.; Simacek, P.; Advani, S. G. (2012): Use of flow simulation to develop robust injection and vent schemes that account for process and material variability in liquid composite molding process. *Computer Modeling in Engineering & Sciences*, vol. 88, no. 3, pp. 155–181.

Wang, V. W.; Hieber, C. A.; Wang, K. K. (1986): Dynamic simulation and graphics for the injection-molding of 3-dimensional thin parts. *Journal of Polymer Engineering*, vol. 7, no. 1, pp. 21–45.

Yang, B.; Fu, X. R.; Yang, W.; Huang, L.; Yang, M. B.; Feng, J. M. (2008): Numerical prediction of phase-change heat conduction of injection-molded high density polyethylene thick-walled parts via the enthalpy transforming model with mushy zone. *Polymer Engineering and Science*, vol. 48, no. 9, pp. 1707–1717.

Yang, B. X.; Ouyang, J.; Jiang, T.; Liu, C. T. (2010): Modeling and simulation of fiber reinforced polymer mold filling process by level set method. *Computer Modeling in Engineering & Sciences*, vol. 63, no. 3, pp. 191–222.

Yang, B. X.; Ouyang, J.; Li, Q.; Zhao, Z. F.; Liu, C. T. (2010): Modeling and simulation of the viscoelastic fluid mold filling process by level set method. *Journal of Non-Newtonian Fluid Mechanics*, vol. 165, no. 19-20, pp. 1275–1293.

Yang, B. X.; Ouyang, J.; Liu, C. T.; Li, Q. (2010): Simulation of non-isothermal injection molding for a non-newtonian fluid by level set method. *Chinese Journal of Chemical Engineering*, vol. 18, no. 4, pp. 600–608.

Zhou, H. M.; Geng, T.; Li, D. Q. (2005): Numerical filling simulation of injection molding based on 3d finite element model. *Journal of Reinforced Plastics and Composites*, vol. 24, no. 8, pp. 823–830.

Zhou, H. M.; Yan, B.; Zhang, Y. (2008): 3d filling simulation of injection molding based on the pg method. *Journal of Materials Processing Technology*, vol. 204, no. 1-3, pp. 475–480.

Zhou, J.; Turng, L. S. (2007): Three-dimensional numerical simulation of injection mold filling with a finite-volume method and parallel computing. *Advances in Polymer Technology*, vol. 25, no. 4, pp. 247–258.